International Journal of Minerals, Metallurgy and Materials
Volume 25, Number 3, March 2018, Page 315
https://doi.org/10.1007/s12613-018-1575-x

Effect of the frequency of high-angle grain boundaries on the corrosion performance of 5wt%Cr steel in a CO_2 aqueous environment

Hui-bin Wu[1,2)], *Tao Wu*[2)], *Gang Niu*[1)], *Tao Li*[3)], *Rui-yan Sun*[3)], *and Yang Gu*[1)]

1) Collaborative Innovation Center of Steel Technology, University of Science and Technology Beijing, Beijing 100083, China
2) National Engineering Research Center of Advanced Rolling, University of Science and Technology Beijing, Beijing 100083, China
3) Survey and Design Institute of Jilin Oilfield Company, Jilin 138000, China
(Received: 10 April 2017; revised: 4 November 2017; accepted: 5 November 2017)

Abstract: The corrosion behavior of 5wt%Cr steel tempered at different temperatures was investigated by immersion testing and electrochemical testing in a CO_2 aqueous environment. When the tempering temperature exceeded 500°C, the corrosion rate increased. The corrosion layers consisted of Cr-rich compounds, which affected the corrosion behaviors of the steels immersed in the corrosive solution. The results of electrochemical experiments demonstrated that 5wt%Cr steels with different microstructures exhibited pre-passivation characteristics that decreased their corrosion rate. Analysis by electron back-scattered diffraction showed that the frequency of high-angle grain boundaries (HAGBs) and the corrosion rate were well-correlated in specimens tempered at different temperatures. The corrosion rate increased with increasing HAGB frequency.

Keywords: chromium steel; grain boundaries; microstructure; corrosion performance; tempering temperature

1. Introduction

CO_2 corrosion is a common and important failure mechanism of components in systems for oil and gas production as well as those for transportation. The mechanism causes not only great economic losses to the oil and gas transportation industry [1] but also environmental pollution. In the field of oil and gas transportation, knowledge of CO_2 corrosion and protection remains immature despite the serious consequences of CO_2 corrosion. Therefore, the investigation and development of oil-casing steels with good mechanical properties and corrosion resistance are important.

In general, the CO_2 corrosion behaviors of carbon steels or low-alloy steels depend on both the physicochemical factors of the surrounding environment (temperature, partial pressure, pH value, solution chemistry, and gas flow rate) and metallurgical variables of the steel material (chemical composition and microstructure) [1]. Material factors include the composition and microstructure of the steel. Differences in chemical composition and manufacturing processes result in steels with different microstructures. The composition and microstructure of the material affect both the mechanical properties and the corrosion behavior under exposure to environmental CO_2.

The mechanism of corrosion resistance in 1wt%–5wt% Cr steels has been studied by numerous researchers. A small amount of Cr (approximately 0.5wt%–5wt%) can substantially improve the corrosion resistance of low-alloy steel to CO_2 [1–7]. The CO_2 corrosion of 5wt% Cr steel has been widely researched because this material is a suitable low-alloy steel with high CO_2 corrosion resistance, excellent mechanical properties, and low cost. For the present study, we obtained 5wt%Cr steels with different microstructures using different tempering processes to explore the influence of microstructure on the corrosion resistance at different tempering temperatures.

Yu *et al.* [8] found that, with increasing tempering temperature, the frequency of low-angle grain boundaries (LAGBs) in Q960 steel decreased gradually. Therefore, the introduction of heat treatment caused substructure formation

Corresponding author: Tao Wu E-mail: wutao940195398@163.com

associated with the rearrangement of dislocations, thereby changing the frequencies of LAGBs and HAGBs [7–11]. Corrosion often occurs preferentially in the higher energy areas surrounding defects [12–13]. Using electron back-scattering diffraction (EBSD), Liang *et al.* [12] found that the dislocation density and low-energy grain boundary both contributed to corrosion resistance. The energy of LAGBs mainly arises from the dislocation energy, and the dislocation density is closely related to orientation differences among grains. Therefore, the energy of an LAGB is also related to the misorientation angle (θ). From the following Eqs. (1) and (2), the LAGB energy (r) increases with increasing orientation difference between the grains. However, the energy of HAGBs is generally stable.

$$r = r_0\theta(A - \ln\theta) \tag{1}$$

$$r_0 = \frac{Gb}{4\pi(1-v)} \tag{2}$$

where G is the shear modulus; v is Poisson's ratio; b is the Burgers vector; and A is an integral constant that depends on the misplaced energy of the center of the dislocation.

The purpose of the present study was to investigate the effect of tempering temperature on the local microstructure and to compare these results with the corrosion behavior of the tempered material. With this approach, the influence of the LAGB/HAGB frequency can be better understood, providing technical support for the development of new weathering steels.

2. Experimental

The experimental materials were made by smelting, forging, controlled rolling, and controlled cooling, i.e., thermomechanical control processes (TMCP), with the following heat treatment: quenching at 930°C, followed by tempering at 200, 500, 600, and 700°C. The major elemental composition of the 5wt%Cr steel was as follows (in wt%): C 0.038, Cr 5.06, Si 0.24, Mn 0.17, Ti 0.017, Ni 0.14, Cu 0.28, P 0.009, S 0.001, Al 0.041, and Nb 0.005 (the balance being Fe).

The microstructures of the samples after tempering were revealed using an etchant of 4vol% nital solution. The surface morphology was observed using a ZEISS ULTRA55 field-emission scanning electron microscope (SEM), which worked at a high voltage of 20 kV, a working distance of 10 mm, and secondary electron imaging mode. The corrosion products were detected using X-ray diffraction (XRD) with Cu K_α radiation and a step size of 0.04°. The crystal phases of the corrosion products were identified by matching the peak positions automatically using the MDI Jade software.

Microhardness testing was conducted on a THV-1MD digital micro-Vickers hardness tester with a load of 4.9 N and a dwell time of 10 s. Room-temperature (25°C) tensile properties of the heat-treated samples were obtained using a CMT5105 tensile testing machine. Three samples were tested for each tempering case. In accordance with the GB/T 228–2002 standard method, standard round-bar tensile specimens with standard gauge distances of 25 mm were cut.

CO_2 corrosion tests were performed in a thermostatic bath at 50°C. The test solution ionic composition (in mg/L) was as follows: SO_4^{2-} 600, HCO_3^- 1000, Mg^{2+} 75, Ca^{2+} 125, and Na^+ 380. The pH value of this solution was 6.18. Prior to weight-loss tests, specimens of 30 mm × 20 mm × 2 mm were polished using successively finer grades of SiC papers reaching 800 grit and were then washed with acetone and anhydrous ethanol. A hole of 3 mm in diameter was machined into each specimen to suspend it in the bath. After immersion for 360 h, the corroded specimens were extracted from the thermostatic bath and immediately rinsed with absolute ethyl alcohol. A chemical dissolution method was used to remove the corrosion layer; the corroded specimen was immersed in a vigorously stirred specific diluted HCl solution (500 mL HCl + 500 mL distilled water + 3.5 g hexamethylenetetramine) for at least 10 min at room temperature [14–15]. Afterward, the corrosion products were removed, rinsed, dried, and reweighed to obtain the final weight of the specimen. The corrosion rate was obtained by the following equation:

$$v = \frac{87600 \times (M_0 - M_t)}{SDt} \tag{3}$$

where v is the average corrosion rate (mm/a); M_0 and M_t are the original and final weights of the specimen (g), respectively; t is the immersion time (h); D is the steel density (g/cm^3); and S is the exposed surface area (cm^2).

Electrochemical measurements were performed with a traditional three-electrode system. Specimens of 10 mm × 10 mm × 4 mm were ground to 2000 grit and then cleaned with distilled water and alcohol. The specimens were used as working electrodes (WEs), a Pt sheet was used as the counter electrode (CE), and a saturated calomel electrode (SCE) was used as the reference electrode (RE). The pH value of the test solution was 6.18. The anode polarization curves were collected by a potentiodynamic sweep technique using a VersaSTAT MC electrochemical workstation.

EBSD was used for the material characterization based on the grain size, crystallographic phase fraction and misorientation angles. A Quanta FEG 450 field-emission scanning electron microscope interfaced with a Nordlys EBSD

detector from Oxford Instruments, which was controlled with the Aztec V2.2 software, was used for data acquisition; the step size was 0.2 μm over an area of 579 μm × 434 μm and the accelerating voltage was 20 kV. Data post-processing was performed using the HKL Channel 5 software. HAGBs were defined as having misorientation angles ≥15°, whereas LAGBs had misorientation angles in the range of $1° \leq \theta < 15°$. The EBSD specimens were prepared by being ground, polished, and electrochemically polished at 25°C and 15.0 V in a solution of 20vol% $HClO_4$ and 80vol% ethanol.

3. Results and discussion

3.1. Microstructural evolution and mechanical properties

The microstructures of 5wt%Cr steel tempered at different temperatures are shown in Fig. 1. The volume fraction of bcc crystal structure, as obtained by EBSD, is 100%. Generally, quenched steel has a martensitic microstructure. The microstructure of the tempered 5wt%Cr steel used in this study comprises mainly tempered martensite. Several martensite blocks exist in the initial austenite grains. Each block contains a colony of parallel martensite laths. The size of the martensite phase does not change significantly for tempering temperatures less than 500°C. When the tempering temperature reaches 600°C, the martensite lath is less stable, becoming further consolidated and roughened. When the tempering temperature reaches 700°C, the characteristics of the martensite laths disappear. In general, with increased tempering temperature, the martensite lath content decreases and the ferrite content increases.

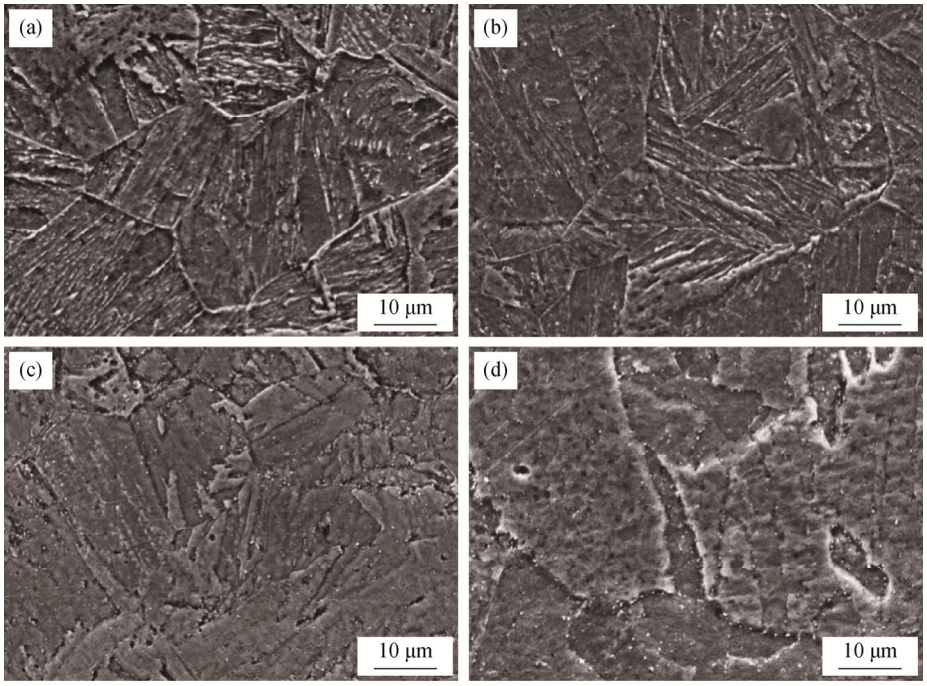

Fig. 1. Microstructure of the 5wt%Cr steel tempered at different temperatures: (a) 200°C; (b) 500°C; (c) 600°C; (d) 700°C.

The measured hardness values from the tempered 5wt%Cr steel are plotted in Fig. 2 as a function of the tempering temperature. Fig. 2 shows that the hardness first increases and then decreases with increasing tempering temperature, reaching the maximum of HV 326.4 at 500°C. Fig. 3 shows the same trends in the yield strength with increasing tempering temperature, reaching a maximum of 842 MPa at 500°C. The tensile strength gradually decreases as the tempering temperature is increased further.

The strength and hardness of martensite are higher than those of ferrite because of solution strengthening by supersaturated C atoms. The martensite structure gradually decreases and the ferrite structure gradually increases with increasing tempering temperature. When the tempering temperature is increased to 500°C, the supersaturation of the martensite decreases and some carbide precipitation occurs. However, the sizes of martensite blocks and laths are not substantially changed with the increases in tempering temperature. From these two factors, hardness and yield strength gradually increase with increasing tempering temperature. However, for tempering temperatures exceeding 500°C, the sizes of martensite blocks and martensite laths change dramatically and the hardness and yield strength rapidly decrease with increasing temperature.

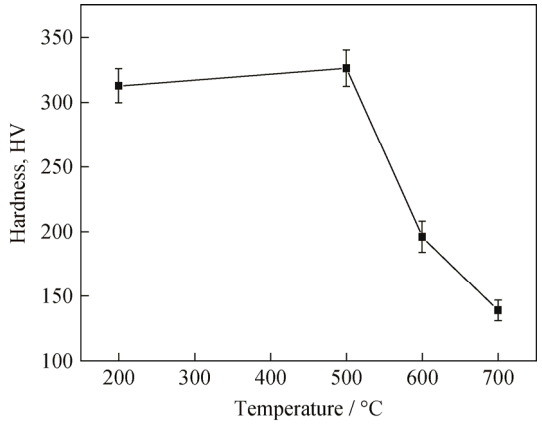

Fig. 2. Trend of hardness with different tempering temperatures.

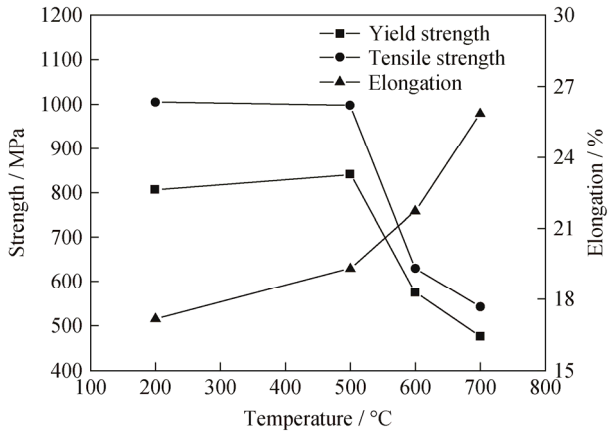

Fig. 3. Trends of yield strength, tensile strength, and elongation of the specimens tempered at different temperatures.

3.2. Corrosion behavior

The average corrosion rates of the samples were measured using a weight-loss method. The surface of 5wt%Cr steel was covered with a uniform and yellow corrosion product. With increasing tempering temperature, the color became darker and the corrosion degree increased. The corrosion rates increase as the tempering temperature is increased (Fig. 4). For tempering temperatures below 500°C, the corrosion rate is relatively low. However, when the tempering temperature reaches 600°C, the corrosion rate increases to 0.0156 mm/a, which is 1.7 times as large as the corrosion rate observed at 200°C.

The polarization curves shown in Fig. 5 vary considerably with increasing tempering temperature. Generally, the curves are shifted to the right without significant changes in shape. Therefore, the corrosion mechanism does not change as the tempering temperature is increased.

The 5wt%Cr steel exhibits significant passivation characteristics. The steels tempered at 200 and 500°C both show stable and evident passive corrosion behavior because they have larger passive areas for anodic polarization potentials exceeding −143 and −107 mV (vs. SCE), respectively. The sample at 200°C has a smaller passivation current density. However, the steels tempered at 600 and 700°C exhibit unstable transient passive corrosion because of their very limited ranges of passive areas.

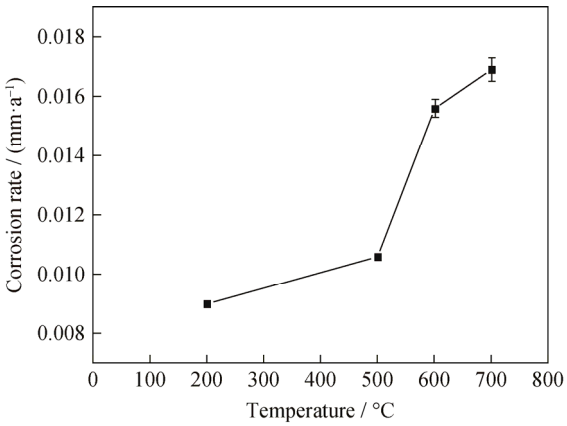

Fig. 4. Average corrosion rate of the samples with different tempering temperatures.

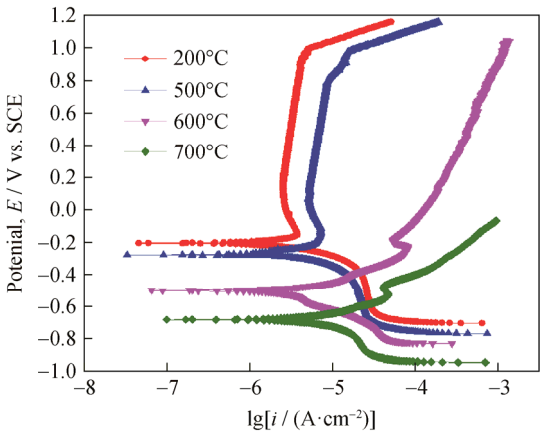

Fig. 5. Polarization curves of the examined samples with different tempering temperatures (the curves were recorded with the samples immersed in electrolyte solution).

The electrochemical parameters of all of the tested specimens were obtained from a Tafel fitting of the potentiodynamic polarization curves; the results are listed in Table 1. These electrochemical parameters include the self-corrosion potential E_{corr}, corrosion current density I_{corr}, anodic Tafel constant β_a, and cathodic Tafel constant β_c. The increases in tempering temperature cause the decreases in corrosion potential and the increases in corrosion current. The results show that, with increasing tempering temperature, the corrosion power and rate both increase.

According to the aforementioned analysis of the corrosion products, the presence of Cr in the steel is necessary to

reduce the corrosion rate. The presence of Cr can improve the passivation capability of steels, thereby enhancing their corrosion resistance. Fe-based alloys containing a minimum content of 12wt% Cr are self-passivating, becoming stainless steels [16]. Previous studies have shown that, although the content of Cr in tested steels remained below 12wt%, passivation clearly occurred.

The Nyquist and Bode plots in Figs. 6 and 7, respectively, were obtained experimentally for the samples tempered at different temperatures. As evident in the results for all of the samples, trends distinguishing the electrochemical corrosion behaviors of particular samples are clearly demonstrated.

Table 1. Parameters of potentiodynamic polarization curves

Tempering temperature / °C	E_{corr} / mV vs. SCE	I_{corr} / (mA·cm^{-2})	β_c / (mV·decade^{-1})	β_a / (mV·decade^{-1})
200	−205.677	1.019	75.4	101.4
500	−264.001	1.055	82.6	114.5
600	−501.681	1.313	47.3	40.3
700	−683.453	3.885	108.5	105.0

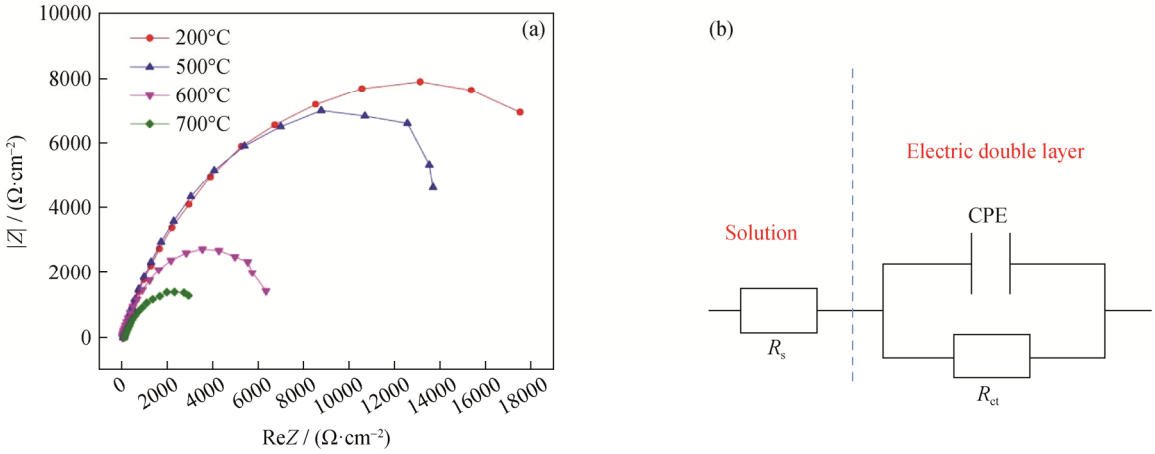

Fig. 6. Nyquist plots (a) and the equivalent electrical circuit of the examined samples (b).

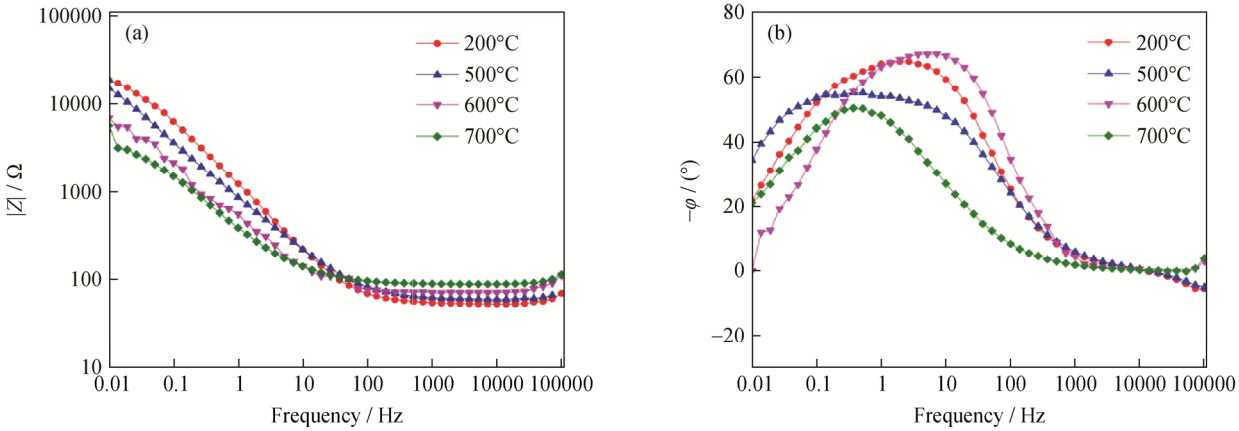

Fig. 7. Bode plots of the examined samples tempered at various temperatures ($|Z|$ is the modulus of impedance; φ is the phase angle): (a) modulus of impedance–frequency; (b) phase angle–frequency.

The Nyquist plots in Fig. 6(a) show significant differences in the four capacitive semicircles corresponding to the samples in CO_2 solution at different tempering temperatures. The impedance spectra of the samples with one time-constant parameter show very large capacitive loops. These loops shrink in the Nyquist plots as the tempering temperature is increased.

At low frequencies between 10^{-2} and 100 Hz, which

represents the polarization resistances of the samples, the modulus of impedance decreases with increasing tempering temperature (Fig. 7(a)). At intermediate frequencies between 100 and 10^4 Hz, the minimum phase angles of the samples tempered at 200 and 500°C are very similar, as the minimum phase angles of the samples tempered at 600 and 700°C (Fig. 7(b)). Thus, the samples exhibit similar double-layer characteristics at 200 and 500°C, or at 600 and 700°C, but distinct differences between these two temperature ranges.

As shown in Fig. 6(b), an equivalent circuit was selected on the basis of the one time-constant parameter characterizing the Bode plots of all of the samples, and the ZSimpWin impedance analysis software was used to determine the impedance parameters. The equivalent circuit was adopted to provide a quantitative analysis of the experimental electrochemical impedance spectroscopy (EIS) results. The equivalent circuit considers the solution resistance (R_s), the charge-transfer resistance (R_{ct}), and the constant-phase element (CPE), which expresses the double-layer capacitance. Because the R_{ct} relates predominantly to the inner barrier layer, this layer apparently provides a barrier to corrosion and a resistance to charge transfer at the interface between the electrolyte and the fresh steel surface.

Fig. 8 shows the microscopic morphologies of the corroded samples in various forms. Corrosion obviously becomes more serious with increasing tempering temperature. Abrading scratches on the specimen surfaces, formed during preparation, are clearly observed, indicating that the rust layer is very thin. Some microcracks in the rust layers are present [17]. These microcracks may be caused by the high growth stress resulting from the volume change between the formed corrosion product and the consumed Fe during the formation of rust layers.

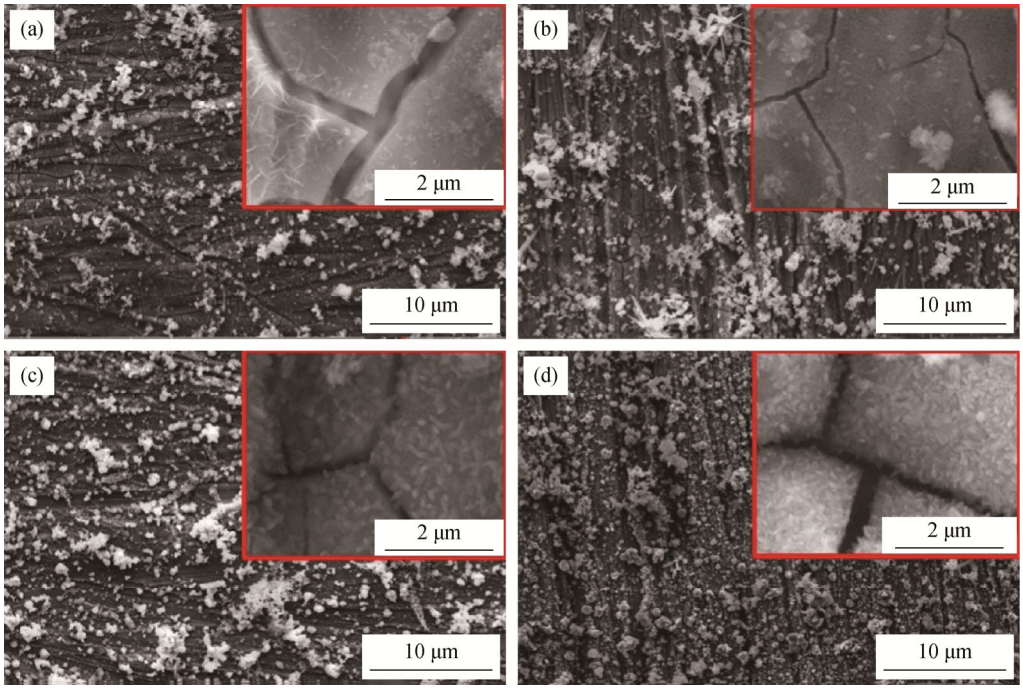

Fig. 8. Microscopic morphologies of corrosion products of the samples tempered at different temperatures: (a) 200°C; (b) 500°C; (c) 600°C; (d) 700°C (the insets present high-magnification images).

SEM images of the corrosion products in Fig. 8 show good agreement with the XRD results in Fig. 9. Previous results have shown that in CO_2 environments with high O_2 concentrations, Fe^{2+} is easily oxidized to Fe^{3+} and the corrosion products of N80 steel comprise $FeCO_3$, Fe_2O_3, and Fe_3O_4 [18]. Fig. 9 presents the XRD patterns of the rust layers formed on various specimens after immersion. In the present study, energy-dispersive X-ray spectroscopy (EDS) and XRD were used to identify the corrosion scale as consisting of Fe_2O_3, $CaCO_3$, goethite (α-FeOOH), and Cr-rich compounds. The scale layers are thin because an intense diffraction peak from the matrix steel (Fe) appears. The C_aCO_3 and Fe_2O_3 offer no good protection because they are distributed porously on the specimen surfaces [19]. However, the inner layer of nano-sized α-FeOOH contains a considerable amount of Cr. Thus, Cr-enriched α-FeOOH is the preferred constituent for a stable and protective rust layer [14]. Some studies [16,20–22] revealed that the main

composition of the steel scale was $Cr(OH)_3$ and $FeCO_3$. After removal from the corrosion bath, cracks in the corrosion products are induced by dehydration [23]. $Cr(OH)_3$ is easily dehydrated to produce Cr_2O_3:

$$Cr + 3H_2O \rightarrow Cr(OH)_3 + 3H^+ + 3e \quad (4)$$

$$2Cr(OH)_3 \rightarrow Cr_2O_3 + 3H_2O \quad (5)$$

The content of Cr in the rust layer is attributed to both its promotion of the formation of a protective rust layer, which acts as a barrier against corrosion processes, and its enhancement of passivation capability, which decreases the anodic dissolution of the substrate alloys. The chemical compositions of the inner rust layer, as determined by EDS, are listed in Table 2. The content of Cr in the inner layer clearly increases with decreased tempering temperature. Thus, with decreasing tempering temperature, the corrosion rust layer becomes more stable and the corrosion rate is decreased. The following electrochemical corrosion reactions occur in the process:

Anodic reaction: $Fe \rightarrow Fe^{2+} + 2e$ (6)

Cathodic reaction: $O_2 + 2H_2O + 4e \rightarrow 4OH^-$ (7)

Total reaction equation: $2Fe + O_2 + 2H_2O \rightarrow 2Fe(OH)_2$ (8)

The transient product $Fe(OH)_2$ can be further oxidized by oxidants and dehydrated to form one or both of the stable corrosion products γ-FeOOH and α-FeOOH.

No obvious $FeCO_3$ crystal is present in the corrosion products, and peaks from $FeCO_3$ are absent in the XRD results. The deposition of $FeCO_3$ is controlled by critical supersaturation. The surface of low-Cr steel often exhibits acidification characteristics [23] that decrease the pH value, thereby greatly increasing the critical supersaturation of $FeCO_3$. Therefore, the amount of deposited $FeCO_3$ decreases [23]. SEM analysis of the corrosion products reveals that many factors influence the kinetics of $FeCO_3$ precipitation, including the pH value and the Fe^{2+} concentration.

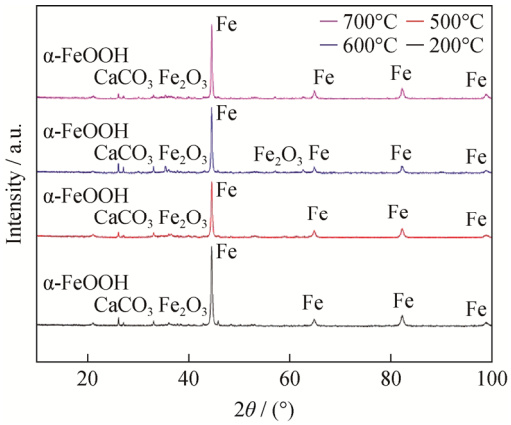

Fig. 9. XRD patterns of the corrosion product layers formed on the samples tempered at different temperatures.

Table 2. Chemical compositions of the inner rust layer samples tempered at different temperatures

Tempering temperature / °C	Cr content		O content		Fe content		Ca content		Mg content	
	wt%	at%	wt%	at%	wt%	at%	wt%	at%	wt%	at%
200	28.10	16.96	28.35	55.62	37.92	21.31	2.29	1.80	3.34	4.31
500	26.42	15.89	25.80	55.70	39.30	22.00	2.01	1.57	3.77	4.85
600	21.64	10.75	42.56	68.72	28.14	13.02	1.50	0.97	6.16	6.54
700	17.65	9.24	38.36	65.22	36.48	17.77	1.43	0.97	6.08	6.80

3.3. Influence of tempering temperature on grain boundaries

Fig. 10 shows the distribution of misorientation angles for 5wt%Cr specimens with different tempering temperatures. In these diagrams, blue, green, red, and black represent misorientation angles of 1°–5°, 6°–10°, 11°–15°, and HAGBs >15°, respectively.

To better understand the evolution of grain boundaries with increasing tempering temperature, we conducted a quantitative statistical analysis using the raw misorientation data in Fig. 10. The frequency evolution of misorientation angles with different tempering temperatures determined in this analysis are shown in Fig. 11. The frequencies of grain boundaries with different misorientation scales are shown in Table 3. The results in Figs. 10 and 11 indicate that the grain-boundary misorientation angles are mostly less than 5°, although the frequency of boundaries in this range decreases with increasing tempering temperature. In the range from approximately 5° to 10°, the frequency of grain boundaries remains nearly constant for tempering temperatures less than 500°C and decreases when the tempering temperature is greater than 500°C. These results are consistent with the variation of martensite laths. The misorientation angles of the martensite lath boundaries are mainly concentrated in the range from approximately 5° to 15°. The frequency evolution of the misorientation angles is strongly correlated with the microstructural evolution.

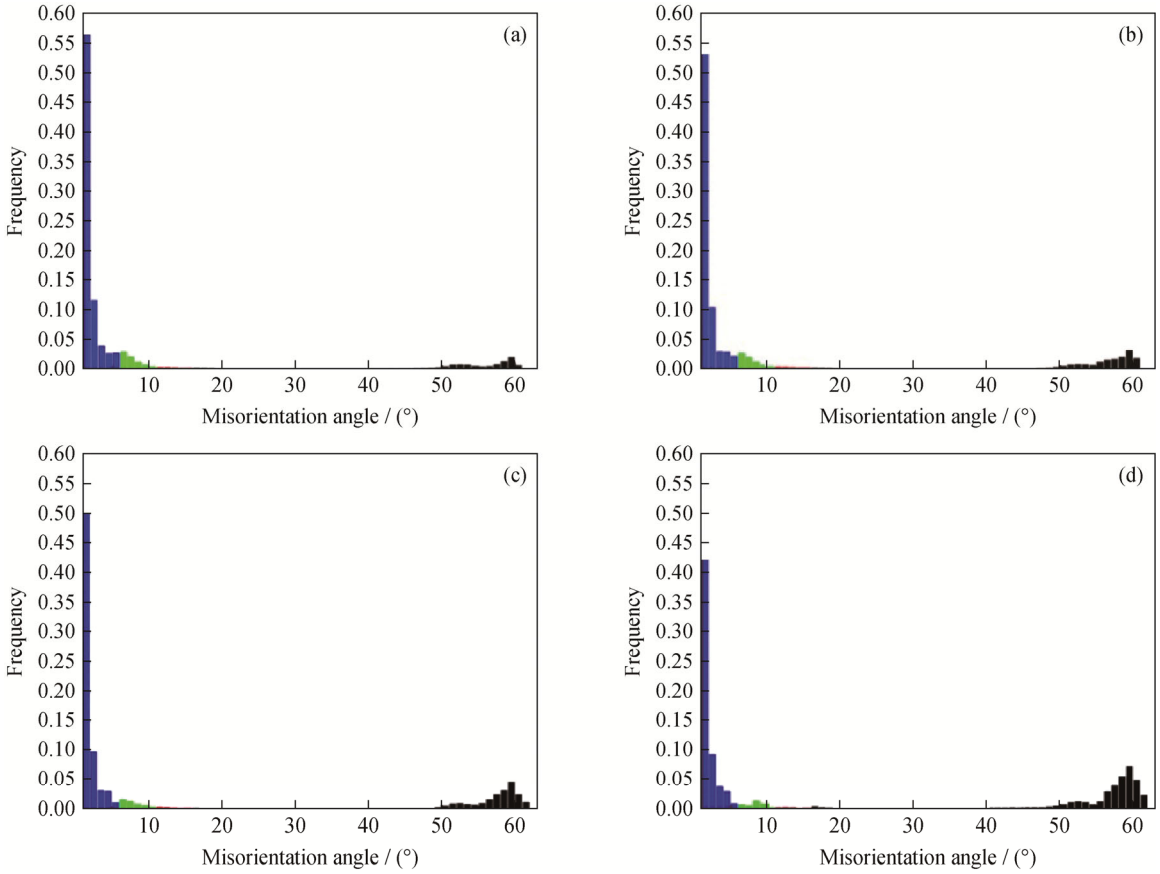

Fig. 10. Distributions of misorientation angles with frequency for different tempering temperatures (blue, green, red, and black represent the misorientation angles of 1°–5°, 6°–10°, 11°–15°, and HAGBs >15°, respectively): (a) 200°C; (b) 500°C; (c) 600°C; (d) 700°C.

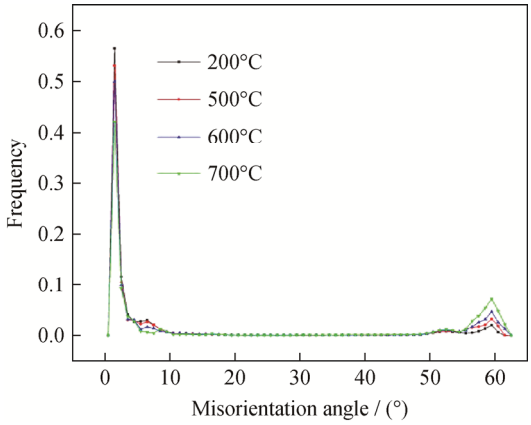

Fig. 11. Frequency evolution with misorientation angles for different tempering temperatures.

Table 3. Frequency of grain boundaries with different misorientation angles

Misorientation angle / (°)	Frequency / %			
	200°C	500°C	600°C	700°C
≤5	77.8	71.8	67.4	58.8
6–10	7.6	7.2	5.1	3.5
11–15	1.6	1.7	1.6	0.9
>15	13.0	19.3	25.9	36.8

3.4. Frequency evolution of HAGB and LAGB

Figs. 12 and 13 indicate that the frequency evolutions of LAGBs and HAGBs are correlated with the increases in tempering temperature. In general, the proportion of LAGBs decreases with increasing tempering temperature. The frequency evolution of HAGBs shows the opposite trend.

3.5. Correlation mechanism between the distribution of HAGBs and corrosion behaviors

Other authors [12] have noted that the frequency of HAGBs in 3wt%Cr steel is lower than that in 1wt%Cr steel; others [13] have reported that the frequency of HAGBs increases with decreasing Cr content of the steel. This experiment shows the same trends, which we attribute to two possible reasons. First, Cr tends to segregate at the boundaries and block the connection of HAGBs. Second, solid solutions of Cr in Fe show significantly reduced stacking-fault energies relative to those of non-Cr-containing steels; many LAGBs appear during the thermal deformation of Cr-containing steels.

The frequency of LAGBs or HAGBs and the corrosion rate show good regularity; the initial corrosion rate increases with increasing frequency of HAGBs. In previous research [12–13],

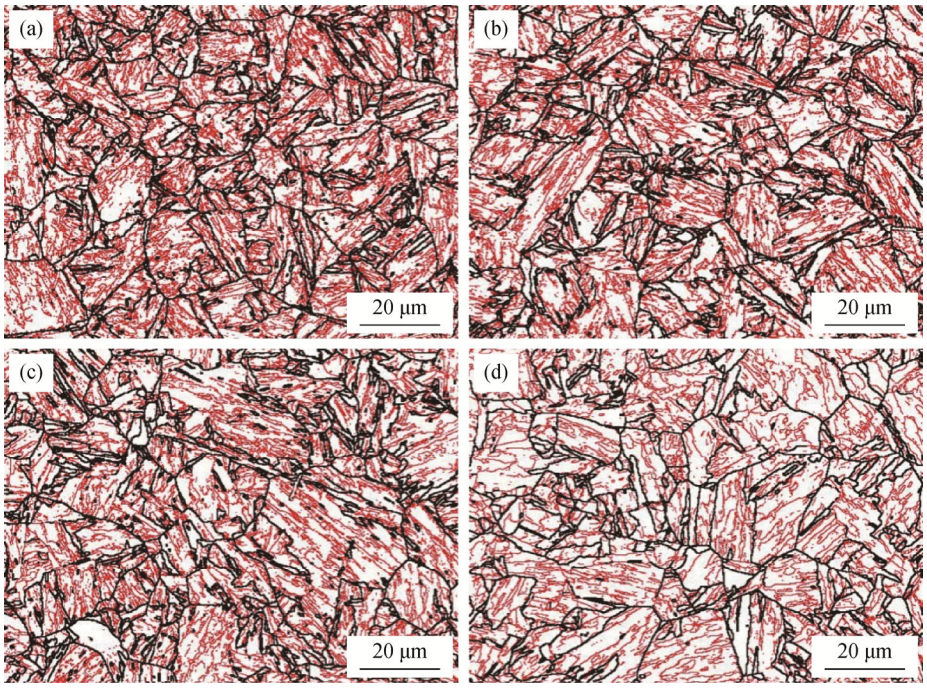

Fig. 12. Distribution evolution of LAGBs (1°–15°, red lines) and HAGBs (>15°, black lines) in samples tempered at different temperatures: (a) 200°C; (b) 500°C; (c) 600°C; (d) 700°C.

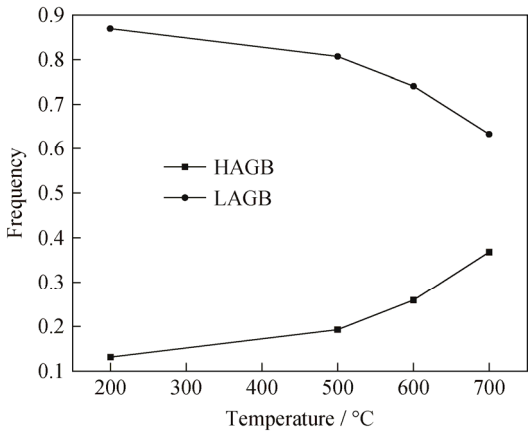

Fig. 13. Frequency evolution of LAGBs and HAGBs as a function of tempering temperature.

the corrosion rate has shown the same regularity. Corrosion tends to initiate and develop in higher-energy locations. As the main defects in the crystal structure, grain boundaries have higher energies; thus, the corrosion tendency is greater at these locations. HAGBs may promote the development of nucleation centers because of their higher energies [10,9]. The structure of LAGBs, which can interrupt HAGB network connectivity, is highly ordered, with a small free volume and a low interfacial energy. LAGBs can effectively block the continuous expansion of material corrosion along HAGBs. Therefore, the initial corrosion rate increases with increasing frequency of HAGBs.

Previous research [16] has shown that dislocation multiplication in the microstructure induced by cold deformation can reduce the Volta potential differences between the ferrite and the austenite phases. Therefore, reducing the LAGB frequency in the microstructure with tempering temperature increasing may increase the Volta potential differences among different grains. The driving force for micro-galvanic interactions between different grains may thereby increase, causing the corrosion rate to increase.

4. Conclusions

(1) The microstructure of tempered 5wt%Cr steel mainly comprises tempered martensite. With the increase of tempering temperature, the martensite lath area decreases and the ferrite content increases. The hardness and yield strength first increase and then decrease as the tempering temperature is increased. Tensile strength gradually decreases as the tempering temperature is increased.

(2) The corrosion products show various microstructural forms. Analysis by EDS and XRD indicates that the corrosion scale consists of Fe_2O_3, $CaCO_3$, goethite (α-FeOOH), and Cr-rich compounds. The content of Cr in the inner layer increases with decreasing tempering temperature; the corrosion rust layer becomes more stable and the corrosion rate decreases.

(3) The frequency evolution of misorientation angles

with variations in tempering temperature is strongly correlated with the microstructural evolution of low-alloy steel. The frequency of HAGBs first increases slowly when the tempering temperature is less than 500°C and then increases rapidly with increasing tempering temperature.

(4) The frequency of LAGB or HAGB is well correlated with the initial corrosion rate, and the corrosion rate of the steel increases with increasing HAGB frequency.

Acknowledgements

This work was financially supported by the National Key R & D Program of China (No. 2017YFB0304900) and the National Science and Technology Major Project of China (No. 2014E-3604).

References

[1] J.B. Sun, W. Liu, and M.X. Lu, Investigation progress of effect of alloying elements and microstructure on CO_2 corrosion behavior of steel, *J. Chin. Soc. Corros. Prot.*, 28(2008), No. 4, p. 246.

[2] W. Li, L.N. Xu, L.J. Qiao, and J.X. Li, Effect of free Cr content on corrosion behavior of 3Cr steels in a CO_2 environment, *Appl. Surf. Sci.*, 425(2017), p. 32.

[3] W. Liu, S.L. Lu, P Zhang, J.J. Dou, and Q.H. Zhao, Effect of silty sand with different sizes on corrosion behavior of 3Cr steel in CO_2 aqueous environment, *Appl. Surf. Sci.*, 379(2016), p. 163.

[4] X.Q. Lin, W. Liu, F. Wu, C.C. Xu, J.J. Dou, and M.X. Lu, Effect of O_2 on corrosion of 3Cr steel in high temperature and high pressure CO_2–O_2 environment, *Appl. Surf. Sci.*, 329(2015), p. 104.

[5] C. Sun, Y. Wang, J.B. Sun, X.Q. Lin, L.D. Li, H.F. Liu, and X.K. Cheng, Effect of impurity on the corrosion behavior of X65 steel in water-saturated supercritical CO_2 system, *J. Supercrit. Fluids*, 116(2016), p. 70.

[6] G.A. Zhang, M.X. Lu, and Y.S Wu, Morphology and microstructure of CO_2 corrosion scales, *Chin. J. Mater. Res.*, 19(2005), No. 5, p. 537.

[7] Z.G. Liu, X.H. Gao, L.X. Du, J.P. Li, C. Yu, R.D.K. Misra, and Y.X. Wang, Comparison of corrosion behaviors of low-alloy pipeline steel exposed to H_2S/CO_2-saturated brine and vapour-saturated H_2S/CO_2 environments, *Electrochim. Acta*, 232(2017), p. 528.

[8] H. Yu, D.D. Zhang, R.T. Xiao, P. Zhou, J.J. Dong, and X.B. Du, Effect of tempering temperature on low angle grain boundaries in Q960 steel, *J. Univ. Sci. Technol. Beijing*, 33(2011), No. 8, p. 952. .

[9] R. Hunag and Y. Han, The effect of SMAT-induced grain refinement and dislocations on the corrosion behavior of Ti–25Nb–3Mo–3Zr–2Sn alloy, *Mater. Sci. Eng. C*, 33(2013), No. 4, p. 2353.

[10] D. Song, A.B. Ma, J.H. Jiang, P.H. Lin, D.H. Yang, and J.F. Fan, Corrosion behaviour of bulk ultra-fine grained AZ91D magnesium alloy fabricated by equal-channel angular pressing, *Corros. Sci.*, 53(2011), No. 1, p. 362.

[11] C. Örnek and D.L. Engelberg, SKPFM measured Volta potential correlated with strain localisation in microstructure to understand corrosion susceptibility of cold-rolled grade 2205 duplex stainless steel, *Corros. Sci.*, 99(2015), p. 164.

[12] J.M. Liang, D. Tang, H.B. Wu, P.C. Zhang, W. Liu, H.Y. Mao, and X.T. Liu, Corrosion behaviors of Cr low-alloy steel in bottom plate environment of cargo oil tanks, *J. South China Univ. Technol. Nat. Sci.*, 41(2013), No. 10, p. 72.

[13] J.M. Liang, D. Tang, H.B. Wu, and L.D. Wang, Environment corrosion behavior of cargo oil tank deck made of Cr-contained low-alloy steel, *J. Southeast Univ. Nat. Sci.*, 43(2013), No. 1, p. 152.

[14] H.E. Townsend, Effects of alloying elements on the corrosion of steel in industrial atmospheres, *Corrosion*, 57(2001), No. 6, p. 497.

[15] T. Nishimura, H. Katayama, K. Noda, and T. Kodama, Effect of Co and Ni on the corrosion behavior of low alloy steels in wet/dry environments, *Corros. Sci.*, 42(2000), No. 9, p. 1611.

[16] L.N. Xu, B. Wang, J.Y. Zhu, W. Li, and Z.Y. Zheng, Effect of Cr content on the corrosion performance of low-Cr alloy steel in a CO_2 environment, *Appl. Surf. Sci.*, 379(2016), p. 39.

[17] Y.H. Qian, C.H. Ma, D. Niu, J.J. Xu, and M.S. Li, Influence of alloyed chromium on the atmospheric corrosion resistance of weathering steels, *Corros. Sci.*, 74(2013), No. 4, p. 424.

[18] C. Ghosh, V.V. Basabe, J.J. Jonas, Y.M. Kim, I.H. Jung, and S. Yue, The dynamic transformation of deformed austenite at temperatures above the Ae_3, *Acta Mater.*, 61(2013), No. 7, p. 2348.

[19] M. Yamashita, H. Miyuki, Y. Matsuda, H. Nagano, and T. Misawa, The long-term growth of the protective rust layer formed on weathering steel by atmospheric corrosion during a quarter of a century, *Corros. Sci.*, 36(1994), No. 2, p. 283.

[20] B. Wang, L.N. Xu, J.Y. Zhu, H. Xiao, and M.X. Lu, Observation and analysis of pseudo-passive film on 6.5%Cr steel in CO_2 corrosion environment, *Corros. Sci.*, 111(2016), p. 711.

[21] S.Q. Guo, L.N. Xu, L. Zhang, W. Chang, and M.X Lu, Corrosion of alloy steels containing 2% chromium in CO_2 environments, *Corros. Sci.*, 63(2012), p. 246.

[22] Z.G. Liu, X.H. Gao, L.X. Du, J.P. Li, Y. Kang, and B. Wu Corrosion behavior of low-alloy steel with martensite/ferrite microstructure at vapor-saturated CO_2 and CO_2-saturated brine conditions, *Appl. Surf. Sci.*, 351(2015), p. 610.

[23] L.N. Xu, B. Wang, and M.X. Lu, Corrosion behavior of 6.5%Cr steel in high temperature and high pressure CO_2 environment, *Acta Metall. Sinica*, 52(2016), No. 6, p. 672.